Published in final edited form as:
Phys Med Biol. 2012 June 7; 57(11): 3435–3449. doi:10.1088/0031-9155/57/11/3435.

Characterization of a high resolution hybrid DOI detector for a dedicated breast PET/CT scanner

Felipe Godinez[1], **Abhijit J. Chaudhari**[2], **Yongfeng Yang**[1], **Richard Farrell**[3], and **Ramsey D. Badawi**[1,2]

[1]Department of Biomedical Engineering, University of California Davis, One Shields Ave, Davis CA 95616, USA

[2]Department of Radiology, UC Davis School of Medicine, Sacramento, CA 95817, USA

[3]Radiation Monitoring Devices Inc, Watertown, MA 02172, USA

Abstract

The aim of this study is to design and test a new high resolution hybrid depth of interaction (DOI) detector for a dedicated breast PET/CT scanner. Two detectors have been designed and built. The completed detectors are based on a 14×14 array of 1.5×1.5×20 mm^3unpolished lutetium orthosilicate (LSO) scintillation crystals, with each element coated in a 50 μm layer of reflective material. The detector is read out from both ends using a position sensitive photomultiplier tube (PSPMT) and a large active area (20 × 20 mm^2) avalanche photodiode (APD) to enable acquisition of DOI information. Nuclear instrumentation modules were used to characterize the detectors' performances in terms of timing, intrinsic spatial resolution (ISR) and energy resolution, as well as DOI resolution with a dual ended readout configuration. Measurements with the APD were performed at a temperature of 10°C. All crystals were identified at all depths, even though the signal amplitude from the PSPMT decreases with depth away from it. We measured a timing resolution of 2.4 ns, and an average energy resolution of 19%. The mean ISR was measured to be 1.2 mm for crystals in the central row of the array for detectors in the face-to-face position. Two off-center positions were measured corresponding to 26° and 51° oblique photon incidence, and the mean ISR at these positions was 1.5 mm and 1.7 mm, respectively. The average DOI resolution across all crystals and depths was measured to be 2.9 mm (including the beam width of 0.6 mm). This detector design shows good promise as a high resolution detector for a dedicated breast PET/CT scanner.

1. Introduction

Breast cancer holds the second highest mortality rate in women over 40 years of age, with an estimated 39,520 deaths in 2011, compared to 71,340 for lung and bronchus cancer (*Cancer Facts and Figures* 2011). This has prompted the growth of breast cancer imaging research, part of which seeks to adapt existing molecular imaging techniques such as positron emission tomography (PET), to dedicated breast imaging through the development of high resolution PET detectors. PET is a technique that uses compounds labeled with positron emitting nuclides, such as ^{18}F-Fluorodeoxyglucose (^{18}F-FDG) to quantify tissue function; and it is routinely the modality of choice in assessing response to therapy, and tumor staging and re-staging of advanced breast cancer (Eubank and Mankoff 2005, Linden et al. 2006).

Initial attempts at imaging the breast with PET were performed using a standard clinical whole body PET (WBPET) scanner (Wahl et al. 1991). However, WBPET poses certain limitations that result in inadequate sensitivity when detecting lesions smaller than 1 cm (Avril et al. 2000): poor spatial resolution, signal loss due to attenuation in the body, and poor annihilation photon sensitivity. To overcome such limitations, dedicated breast PET

(DbPET) systems are designed to improve spatial resolution by reducing the scintillator pixel size, increasing sensitivity by bringing the detector closer to the breast, and reducing body attenuation effects by scanning only the breast.

Examples of such specialized detectors are found in Positron Emission Mammography (PEM) systems (Thompson 1994, Moses 1995). PEM systems make use of planar detectors, which can be integrated into paddles used to compress the breast during PEM. There are several PEM systems under development (Murthy et al. 2000, Rosen et al. 2005, Karimian et al. 2005, Wang et al. 2006) and one system is commercially available (Weinberg et al. 2004, Springer and Mawlawi 2011). However, spatial resolution gains from PEM detectors are reduced by the geometrical configuration in which they are implemented. As a consequence PEM cannot fully tomographically sample the breast, resulting in artifacts (Smith et al. 2003) and the degradation of spatial resolution between planes parallel to the compression paddles (or the z-direction), where the resolution tends to be ~8 mm (MacDonald et al. 2009). Another related cause of spatial resolution degradation effecting both planar and circular detector geometries is the parallax error. In PEM, parallax error progressively blurs the in-plane spatial resolution towards the center of the field of view (FOV). A detailed explanation of parallax error in general can be found in Cherry et al. (2003). Fortunately, parallax error can be corrected if the depth along the crystal length, where the annihilation photon interacted, is known. This implies that detectors with the capability to encode the depth of interaction (DOI) are necessary for maintaining a uniform spatial resolution across the FOV.

DbPET systems capable of complete tomographic sampling image the patient in the prone position allowing the breast to hang pendant with minimal patient discomfort. In DbPET systems, detectors are placed in close proximity to the breast and either encircle it or rotate around it. Several DbPET systems have been built or are under development (Huber et al. 2006, Tai et al. 2008, Albuquerque et al. 2008, Ravindranath et al. 2008, Furuta et al. 2009, Bowen et al. 2009, Moliner et al. 2010, Kitamura et al. 2010, Raylman et al. 2011). Parallax error is the prime limitation in these geometries, due to the use of long crystals designed for increased 511 keV photon detection efficiency and their proximity to the object. Therefore, DOI detectors are the desired detector type for DbPET systems.

1.1. Detectors for depth of interaction encoding

The majority of DOI detector configurations can be categorized as, but are not limited to, single-ended or dual-ended crystal readouts. See Ito et al. (2011) for a review of DOI detector designs. A major drawback of single-ended readout detectors tends to be their poor DOI resolution (4-8mm) (Yang et al. 2009). Dual-ended readout detectors can achieve greater DOI resolution with better light collection efficiency. Photomultiplier tubes (PMT) are large and bulky, hence, the use of photodiode arrays and avalanche photodiodes (APDs) in a dual ended readout configuration has been considered and investigated (Moses et al. 1995, Gramsch 1996). Yang et al.(2006) reported an average DOI resolution of 3.4 mm for a 5×5 array of 1.5×1.5×20 mm^3 coupled to two PSAPDs, and an energy resolution of 15% .

Although the DOI configuration with the PSAPD dual-ended readout can achieve a high DOI resolution and provide a compact form factor, this configuration is limited in coincidence timing performance. It has been shown that such a configuration could have a coincidence timing resolution of 9.9 ns (Yang et al. 2008). This is a serious limitation in breast imaging since a significant portion of the radiotracer is located outside the FOV, increasing the random coincidence rate (Bowen et al. 2006). A hybrid dual-ended DOI detector with a PMT and PSAPD can improve the coincidence timing resolution if the coincidence trigger is taken from the faster PMT detector. Hybrid detectors have been measured to have DOI resolutions in the range of 3-6mm (Chaudhari et al. 2008).

1.2. Detector under investigation

The hybrid detector being investigated in this work is designed to achieve high sensitivity while retaining uniform spatial resolution across the field of view, and at the same time be capable of optimal operation in the high flux environments likely to be encountered in breast imaging. This detector is expected to have a timing performance of a PMT based detector with the added benefit of dual-ended DOI encoding. To this end the detector is configured for DOI encoding with an APD on the patient end, and a position sensitive PMT (PSPMT) on the opposite end (figure 1). The PSPMT is used to resolve event positions in the XY plane (that is, crystal identification), and it also serves as the coincidence triggering device. The APD serves only as a spectroscopy detector without spatial information. Its thin and low attenuating body is favorable for placement at the patient end, allowing a high detector packing fraction. The packing fraction can be high because the selected APD has an area smaller than the scintillation crystal array face area, avoiding any overhang. The crystal array was chosen to be of lutetium orthosilicate (LSO) for its fast and high light output (Daghighian et al. 1993). The crystals were polished at the ends and unpolished on the sides, with diffuse reflector on the 4 lateral faces. It is well known that unpolished crystals with a diffuse reflector have increased light loss compared to polished crystalswith specular reflectors (Shao et al. 2002), and hence, they are better suited for DOI encoding (Yang and Dokhale 2006). This article reports the following characteristics of the hybrid detector for being implemented into a full ring breast PET system: timing resolution, energy resolution, DOI resolution, and intrinsic spatial resolution (ISR).

2. Materials and Methods

2.1. Detector fabrication

The scintillator was manufactured from LSO (Siemens, Knoxville, TN). The 14 × 14 array of 1.5 × 1.5 × 20 mm^3 LSO crystals was saw cut and left unpolished with 50 μm thick Toray (Toray Industries Inc., Tokyo, Japan) reflector bonded between crystals on lateral faces and on four external array faces (Agile Engineering Inc., Knoxville, TN). The final size of the array was 22 × 22 × 20 mm^3 including reflector material. A PSPMT (R8900-00-C12, Hamamatsu Photonics, Iwata, Japan) was coupled to the end face of the scintillator array with optical grease (BC-630, Saint-Gobian Crystals, Hiram, OH) and the other end was coupled to a custom large active area planar (non-pixelated) PSAPD (Radiation Monitoring Devices, Watertown, MA) with optical grease (figure 1). A faraday cage was built directly on the PSPMT to eliminate electromagnetic field interference from the PSPMT to the PSAPD preamps. A copper foil 0.0029 inch thick (Part: 76555A726, McMaster-Carr, USA) with a non-conductive side was wrapped around the PSPMT steel case, and a transparent stainless steel mesh with a wire diameter of 0.0012 inch (50 Mesh T316, TWP Inc., Berkeley, CA) was placed over the PSPMT entrance window and soldered to the copper foil. The faraday cage was grounded on the PSPMT preamp boards. The PSAPD was operated like an APD by connecting the four position information pins together (herein the PSAPD will be termed APD), since only the energy information was needed.

The active area of the APD is 20 × 20 mm^2 is slightly smaller than the LSO array; because of this the APD only samples half the crystal for edge crystals and only a quarter crystal for corner crystals (see section 1.2). The active area of the PSPMT is 23.5 × 23.5 mm^2 and it was read out by preamp boards purchased from Siemens (Part: 10097920, Siemens Medical Solutions, Hoffman Estates, IL). The 12 anode signals from the C12 PSPMT were mapped onto 4 channels by a resistive network (Seidel et al. 1999a). The APD is read out with a preamp board designed and fabricated by our group according to Shah et al. (2002, 2004).

The active area of the APD used in this work was 2.0 times larger than the largest APD of this type used in a PET detector to date (Yang et al. 2011), and as such suffers from higher noise. The noise level increases with active area; for example at room temperature an active area of 14 × 14 mm^2 has a measured noise level of 130 electron-rms (Shah et al. 2002) compared to 175 electron-rms (RMD, personal communication, March 2, 2012) for a 20 × 20 mm^2 active area. To improve gain and reduce noise the APD was cooled to 10°C for all measurements. Cooling was achieved by flowing chilled dry-air (XR401 Air-Jet, FTS Systems, SP Industries, Stone Ridge, NY) into the closed plastic detector housing. Both detector signals were processed using nuclear instrumentation modules.

2.2. Coincidence timing resolution

Two detector modules were assembled and coincidence data were acquired using a data acquisition (DAQ) board (PD2-MFS-8-500k/14, UEI, Inc., Canton, MA, USA). A 2.5 cm diameter cylindrical ^{68}Ge positron-emitting source (Eckert & Ziegler, Valencia CA, USA) was placed between them. The PSPMT channel sum pulse, of each detector, was passed through a constant fraction discriminator (CFD) and qualified events were fed into a linear fan in/fan out. One CFD output from each detector was sent to a logic unit for coincidence check. The other was sent to a time to amplitude converter (TAC) as the start trigger. The second detector pulse from the CFD, after coincidence, was sent to the TAC as the stop trigger. At 15 minutes after the measurement was started, the stop trigger was delayed by 20 ns in order to create a second timing peak for calibration purposes. The acquired data was plotted and fitted with a Gaussian function to determine the timing peak full width at half maximum (FWHM).

2.3. Flood histograms and DOI

DOI resolution was measured with a single detector module and an electronically collimated fan beam of annihilation photons, as shown in figure 2. The LSO array was irradiated from the side with a fan beam 0.6 mm wide (at the crystal array entry point) at five depths, 4 mm apart starting at 2 mm from the PSPMT-array coupling. The fan beam was created by only accepting coincident events from a 0.25 mm ^{22}Na point source (Eckert & Ziegler, Valencia CA, USA) between a 0.6 × 32 × 20 mm^3 LSO slab coupled to a single channel PMT (Hamamatsu, R580) and the PSPMT coupled to the LSO array (Figure 2). The fan beam was made wide enough in the transaxial plane (parallel to the PSPMT entrance window) to irradiate all the crystals in the array at a given depth. The summed value of the four PSPMT mapped channels is proportional to the deposited energy, and was passed through a CFD with a threshold just above noise. After being thresholded, the summed pulse was sent to a logic unit for coincidence check with the single channel PMT pulse. PSPMT coincidence ($2\tau = 8ns$ window) events were then sent to a trigger guard with a 10 μs delay.

The trigger guard was created by increasing the CFD trigger width with a delay and trigger generator. This was in place to prevent the loss of synchronization between the two DAQ boards (Judenhofer et al. 2005), thus avoiding misaligned events between the PSPMT and APD. The PSPMT DAQ board was triggered by the trigger guard output, which coincided in time with the coincidence logic unit trigger. The amplitude of the 4 PSPMT channel signals were digitized and list mode data recorded. The APD channel was fed directly to a second and separate DAQ board for processing, triggered by the delayed (300 ns) PSPMT trigger. Two DAQ boards with separate triggers were required since the PSAPD charge collection is slower than the PSPMT's (Chaudhari et al. 2008). The delay was selected such that the PSPMT trigger edge coincided with the peak of the shaped APD signal. Each acquisition collected 1 million counts. Two detector blocks were characterized in order to carry out the intrinsic ~spatial resolution measurement described in section 2.4.2.

2.4. Energy and DOI resolution

The pulse height spectrum of unpolished crystals is highly dependent on crystal depth such that without DOI information the energy resolution measurement may be sub-optimal because a clear photopeak may not be identifiable. Hence the energy resolution was measured using the same setup as for DOI resolution. The total energy deposition for a single event was determined as the sum of the summed PSPMT signals and the APD signal after gain calibration. The total event energy was used to measure the energy FWHM.

All raw data was analyzed using the process described by Chaudhari et al. (2008). In brief: for each crystal a gain calibration constant, k, was determined, in order to correct for differences in gain between the PSPMT and the APD. This constant was calculated by taking the ratio of the central depth peak position in individual energy spectra collected for the same crystal by the PSPMT and APD. The DOI position estimate was calculated as $kPSPMT(APD + kPSPMT)$; the ratio of the PSPMT energy over the summed total energy of both the PSPMT and APD.

2.4.1. Repeatability of DOI measurement—To test the precision of the DOI measurement, it was repeated 3 times. At each iteration the experimental setup was completely disassembled and then reassembled. This was done using a 2 mm wide crystal slab for electronic collimation instead of the 0.6 mm. The thicker slab was used to avoid breaking the fragile thinner slab during the disassembly and reassembly process, and to shorten the data acquisition time.

2.4.2. Intrinsic spatial resolution—The intrinsic spatial resolution (ISR) was measured using the technique described by (Dokhale et al. 2006), assuming a detector ring diameter of 21 cm. In summary, the ISR was measured with the two detector blocks in three orientations: face-to-face with gamma rays incident at 90°, oblique with incident ray at 26° (45 mm radial offset) and 51° (81 mm radial offset), corresponding to 78% FOV of the 21 cm diameter ring of detectors (Figure 3(a)). For the face-to-face ISR measurement at the center of the FOV, the 0.25 mm point source was stepped across the arrays in 0.1 mm intervals. Two cases were examined in the oblique positions (1) the case where DOI information was used, and (2) the case where DOI information was omitted. For the off-center measurements the source was stepped in 0.3 mm intervals. This stepping process was used for the DOI omitted case. The ISR forthe off-center measurements where the DOI information was used, was determined by back-projecting lines of response (LOR) from a central crystal in each detector (Figure 3(b)). The annihilation photon interaction positions were calculated using the continuous DOI information from each detector. The DOI corrected ISR was determined from a profile through the intersection of all the measured LORs for a point source at single radial position. Three point source positions were analyzed to determine an average ISR with DOI correction.

3. Results

3.1. Crystal identification

A flood histogram was created for each DOI depth and from coincidence timing measurement data. Identification of all 196 crystals was possible in the flood histograms from the timing data set and for all DOI depths, except for the one nearest the PSAPD. Near the PSAPD, the edge and corner crystals are not fully delineated due to decreased light collection by the PSPMT. However, crystal segmentation is still possible by the automated segmentation algorithm we used (Chaudhari et al. 2008b). This method computes the crystal boundaries using a flood histogram from the 2 mm depth (nearest the PSPMT) position, which has fully defined crystal centers. The algorithm then deforms the template and

registers it to the other floods to obtain a segmentation. An overlay of the segmentation over the flood histogram is shown in figure 4(a). By comparing figure 4(b), (c), and (d); it is clear that the corner and edge crystals are less identifiable at depths furthest from the PSPMT; however, all inner crystals are fully resolved. Also, given the nature of the DOI experimental setup, crystals further from the point source recorded fewer events, as can be seen in the floods in figures 4(b)-(d). For the purpose of visualizing low count crystals, a histogram equalization process was applied to the flood histograms (Figure 4 (e)-(g)).

3.2. Timing resolution

Figure 5 shows the coincidence timing spectrum for the entire array. Crystal-wise timing resolution is shown in figure 6. The average crystal timing resolution is $2.3 \pm 0.02 ns$. The asymmetry in the left hand side of the curve in figure 5 may be caused by differences in the detector's readout electronics and their corresponding NIM electronics processing (Knoll 2000). This asymmetry is also seen in Moses and Derenzo (1999).

3.3. DOI resolution

The crystal-wise DOI resolution averages are tabulated in table 1. The DOI resolution averaged over all depths and crystals is 2.9 mm. It is noted that the best DOI resolution is found at the ends of the array nearest the photodetectors, with the poorest at the middle depth. Figure 7 shows the DOI profiles at 5 depths along the crystal length for a center crystal. For this center crystal the mean FWHM is 2.6 mm and the mean FWTM is 9.7 mm. The relation between the calculated DOI position and the known DOI position was found to be linear and uniform across crystals. A linear fit to the data resulted in a mean R^2 of 0.996 across all crystals with a standard deviation of 0.0314. The precision of the experimental setup to measure DOI and energy resolution for all crystals in the array was high with a standard deviation of 0.12 mm and 0.64%, respectively (Table 2). Figure 8 shows the average DOI resolution across crystals at each sampled depth. The inner crystals have the best and most uniform DOI resolution in the array. The corner crystals are slightly worse than the edge crystals, and the edge crystals have a poorer DOI resolution than the inner crystals. This is mainly a result of the APD partially sampling the edge and corner crystals.

3.4. Energy resolution

The energy resolution (ER) was measured for every depth and crystal. The ER averages over all crystals and depths are shown in table 1. The average ER over all depths for inner (12×12) crystals is 19.1% and 21.6% for all crystals. Figure 9 shows the average ER resolution across crystals at each sampled depth. The crystals were sorted into three crystal groups: inner crystals, edge crystals, and corner crystals. The energy resolution averaged across depths for each crystal group is: 19.1%, 28.2%, and 32.8 %, respectively. The error bars indicate the standard deviation across crystals in a given group. It can be seen that the ER progressively degrades closer to either photodetector and it is best in the middle (see figure 9). This can be explained by considering that the amount of light collected by either photodetector decreases as the distance from the interaction point to the photodetector increases. Thus the combined energy resolution is best where most of the light produced by the scintillation event is collected by both detectors, in this case the middle. For a central crystal, the individual measured ER for the PSPMT ranges from 23.2%-26.1% depending on depth. Likewise, the ER for the APD ranges from 21.8%-32.0%.

3.5. Intrinsic spatial resolution

The intrinsic spatial resolution at the center of the FOV is shown in figure 10 for a central row of crystals. The mean ISR is 1.2 mm with a range of 1.1 mm - 1.3 mm and the corresponding mean FWTM is 2.66 mm with a range of 2.0 mm - 2.9 mm. This ISR value

represents the best ISR possible for the entire system. The outer crystals have the highest ISR but also have fewer counts. This is attributed to the fact that edge crystals receive less inter-crystal scatter than central crystals that are surrounded by other crystals. Near the edge of the FOV the ISR is expected to degrade if parallax is not corrected. The ISR at 26° oblique with no DOI corrections is ~4 mm (figure 11(a)). At the 51° position, where the ISR degradation due to parallax is more pronounced, the ISR without DOI correction is ~6 mm (figure 11(b)). When DOI corrected, the mean ISR at 26° and 51° for a single central crystal is 1.5 mm and 1.7 mm, respectively (figure 12). The mean FWTM at these same positions is 3.3 mmand 3.8 mm, respectively.

4. Discussion

A hybrid detector with DOI capability is characterized for implementation in the next generation DbPET system at UC Davis. This detector is expected to have a timing performance of a PMT based detector with the added benefit of dual-ended DOI encoding.

Although the active area of the PSAPD is not large enough to completely sample the edge and corner crystals, it was possible to calculate DOI and ER values for them based on optical crosstalk with inner crystals. Furthermore, to address this issue we are currently investigating the use of even larger APDs that fully sample all crystals in the array. Preliminary measurements have shown that with a larger APD theedge and corner crystals perform as well as inner crystals. The disadvantage of this arrangement is that the APD packaging overhangs the front face of the crystal array resulting in a loss of geometrical efficiency. However, in the current detector packing fraction is limited primarily by the PSPMT size and the readout stack, because they are larger than the crystal array and the APD. Axially, the PSPMT readout boards require that the crystal arrays be separated by 12 mm, but in the transaxial direction the separation between the edges of the array front face is small, limited primarily by the APD. This implies that the APD does not effect packing fraction in the axial direction. If the current APDs are used, the transaxial packing fraction is optimized for a ring radius of 10 cm, allowing the crystal array front face edges to make contact while the PSPMT envelope edges are also in contact.

In breast imaging, ER is important since only a small fraction of the injected activity accumulates in the breast lesion, while a majority of the activity is outside the FOV. Thus, random coincidence events are more probable in this scenario than in whole body PET (Bowen et al. 2006). The greater contribution from randoms in breast imaging can be reduced using a narrower energy window, which requires a good ER to maintain the noise equivalent count rate. The current DbPET at UCDavis is known to have an ER ranging from 18% to 40% and an average ER of 25% (Wu et al. 2006). The detector investigated here improves this value to a mean ER of 19% with a reduced variation. The ER attained with this detector is worse than expected for typical PET detectors based on LSO because the crystals are unpolished; thus, ER is traded-off for improved DOI (Shao et al. 2002). The random coincidences can also be reduced by implementing a narrow coincidence timing window. Given the 2.3 ns coincidence timing resolution measured this narrow window can be achieved. More work to reduce this further is ongoing.

Spatial resolution is made more homogenous in the FOV when DOI is implemented and therefore it is improved. This is important in breast imaging where the detectors are as close as possible to the breast. This hybrid detector will allow for DOI encoding with a resolution of ~3.0 mm. At the patient end of the detector where the majority of interactions are expected the DOI is ~2.0 mm. Implementationof the DOI information in this detector has shown to improve the ISR at the edge of the FOV from 6 mm to 1.7 mm. Comparing these

ISR figures (the DOI case and the DOI omitted case) serves only as an engineering check, since the methods used to determine the ISR in each case are different.

Implementing this hybrid design will present some data acquisition complications in a complete scanner. The results measured here were obtained using NIM electronics, which can easily be configured with multiple trigger outputs. However, the DAQ electronics (Cardinal, Siemens Corp.) considered for the system design are optimized for single detector triggers, and will require modifications to handle the charge collection delay of the APD.

5. Conclusion

In conclusion, we have characterized a detector design for use in a breast PET scanner. This design will improve on spatial resolution and uniformity across the FOV compared to our current prototype (Wu et al. 2009). The detector configuration will allow for a ring diameter of 20 cm with no gaps between the front faces of the detectors, provided that the detector envelope is of minimal thickness. In practice we expect the envelope to have a thickness of 1.5 mm. Additionally, the combination of the coincidence timing resolution and the fast readout electronics to be used results in a scanner capable of effectively operating in the expected high singles flux (Bowen et al. 2009).

Acknowledgments

The authors would like to thank Drs William Moses and Sara St James for useful discussions, and Drs Yibao Wu and Martin Judenhofer for assistance with electronics and data acquisition software. Funding for this work was provided by NCI R01 CA129561, NCI T32 EB003827-5, and NCI F31 CA157213

References

Albuquerque, E.; Almeida, FG.; Almeida, P., et al. An overview of the clear-pem breast imaging scanner; Nuclear Science Symposium Conference Record, 2008. NSS ’08. IEEE; 2008; p. 5616-5618.

Avril N, Rose CA, Schelling M, Dose J, Kuhn W, Bense S, Weber W, Ziegler S, Graeff H, Schwaiger M. Breast imaging with positron emission tomography and fluorine-18 fluorodeoxyglucose: use and limitations. J Clin Oncol. 2000; 18(20):3495–502. [PubMed: 11032590]

Bowen SL, Wu Y, Chaudhari AJ, Fu L, Packard NJ, Burkett GW, Yang K, Lindfors KK, Shelton DK, Hagge R, Borowsky AD, Martinez SR, Qi J, Boone JM, Cherry SR, Badawi RD. Initial characterization of a dedicated breast PET/CT scanner during human imaging. J Nucl Med. 2009; 50(9):1401–8. [PubMed: 19690029]

Bowen, SL.; Yang, Y.; Wu, Y.; Cherry, SR.; Boone, JM.; Moses, WW.; Badawi, RD. Monte carlo simulation study of several camera designs for the PET component of a dedicated breast PET/CT scanner; IEEE Nuclear Science Symposium Conference Record, 2006; IEEE. 2006; p. 3920-3924.

Cancer Facts and Figures. Technical report American Cancer Society; 2011.

Chaudhari AJ, Joshi AA, Bowen SL, Leahy RM, Cherry SR, Badawi RD. Crystal identification in positron emission tomography using nonrigid registration to a fourier-based template. Phys. Med. Biol. 2008b; 53(18):5011–5027. [PubMed: 18723924]

Chaudhari AJ, Yang Y, Farrell R, Dokhale PA, Shah KS, Cherry SR, Badawi RD. PSPMT/APD hybrid DOI detectors for the PET component of a dedicated breast pET/CT system - a feasibility study. IEEE Transactions on Nuclear Science. 2008; 55(3):853–861.

Cherry, SR.; Sorenson, JA.; Phelps, ME. Physics in Nuclear Medicine. 3rd edn. Saunders; 2003.

Daghighian F, Shenderov P, Pentlow KS, Graham MC, Eshaghian B, Melcher CL, Schweitzer JS. EVALUATION OF CERIUM-DOPED LUTETIUM OXYORTHOSILICATE (LSO) SCINTILLATION CRYSTAL FOR PET. IEEE Trans. Nucl. Sci. 1993; 40(4):1045–1047.

Dokhale PA, Silverman RW, Shah KS, Farrell R, McClish MA, Entine G, Cherry SR. Intrinsic spatial resolution and parallax correction using Depth-Encoding PET detector modules based on Position-Sensitive APD readout. IEEE Transactions on Nuclear Science. 2006; 53(5):2666–2670.

Eubank WB, Mankoff DA. Evolving role of positron emission tomography in breast cancer imaging. Semin Nucl Med. 2005; 35(2):84–99. [PubMed: 15765372]

Furuta, M.; Kitamura, K.; Ohi, J.; Tonami, H.; Yamada, Y.; Furumiya, T.; Satoh, M.; Tsuda, T.; Nakazawa, M.; Hashizume, N.; Yamakawa, Y.; Kawashima, A.; Kumazawa, Y. Basic evaluation of a c-shaped breast PET scanner; Nuclear Science Symposium Conference Record (NSS/MIC), 2009 IEEE; 2009; p. 2548-2552.

Gramsch, EG. Operating characteristics of avalanche photodiodes for PET systems; Nuclear Science Symposium Conference Record. 1996, IEEE; 1996; p. 768-772.

Huber JS, Moses WW, Wang GC, Derenzo SE, Huesman RH, Qi JY, Virador P, Choong NS, Mandelli E, Beuville E, Pedrali-Noy M, Krieger B, Meddeler GJ. A retrospective on the LBNL PEM project. Phys. Medica. 2006; 21:60–63.

Ito M, Hong SJ, Lee JS. Positron emission tomography (PET) detectors with depth-of-interaction (DOI) capability. Biomedical Engineering Letters. 2011; 1(2):70–81.

Judenhofer MS, Pichler BJ, Cherry SR. Evaluation of high performance data acquisition boards for simultaneous sampling of fast signals from PET detectors. Phys. Med. Biol. 2005; 50(1):29–44. [PubMed: 15715420]

Karimian A, Thompson C, Sarkar S, Raisali G, Pani R, Davilu H, Sardari D. CYBPET: a cylindrical PET system for breast imaging. Nuclear Instruments and Methods in Physics Research Section A: Accelerators, Spectrometers, Detectors and Associated Equipment. 2005; 545(1-2):427–435.

Kitamura, K.; Satoh, M.; Furuta, M.; Nakamoto, Y. First clinical trials of dedicated breast PET scanners; 2010 World Molecular Imaging Congress, Abstracts; World Molecular Imaging Congress Kyoto Japan. 2010;

Knoll, GF. Radiation detection and measurement. 3rd edn. Wiley; 2000.

Linden HM, Stekhova SA, Link JM, Gralow JR, Livingston RB, Ellis GK, Petra PH, Peterson LM, Schubert EK, Dunnwald LK, Krohn KA, Mankoff DA. Quantitative fluoroestradiol positron emission tomography imaging predicts response to endocrine treatment in breast cancer. J Clin Oncol. 2006; 24(18):2793–2799. [PubMed: 16682724]

MacDonald L, Edwards J, Lewellen T, Haseley D, Rogers J, Kinahan P. Clinical imaging characteristics of the positron emission mammography camera: PEM flex solo II. Journal of Nuclear Medicine. 2009; 50(10):1666–1675. [PubMed: 19759118]

Moliner, L.; Benlloch, JM.; Carles, M.; Correcher, C.; Gonzalez, AJ.; Orero, A.; Sanchez, F.; Soriano, A. Performance characteristics of the MAMMI PEMT scanner based on NEMA NU 2-2007; Nuclear Science Symposium Conference Record (NSS/MIC), 2010 IEEE; 2010; p. 2591-2594.

Moses WW, Budinger T. PET camera designs for imaging breast cancer and axillary node involvement. 1995; 36:69.

Moses WW, Derenzo SE. Prospects for time-of-flight PET using LSO scintillator. IEEE Transactions on Nuclear Science. 1999; 46(3):474–478.

Moses WW, Derenzo SE, Melcher CL, Manente RA. ROOM-TEMPERATURE LSO PIN PHOTODIODE PET DETECTOR MODULE THAT MEASURES DEPTH OF INTERACTION. IEEE Trans. Nucl. Sci. 1995; 42(4):1085–1089.

Murthy K, Aznar M, Thompson CJ, Loutfi A, Lisbona R, Gagnon JH. Results of preliminary clinical trials of the positron emission mammography system PEM-I: a dedicated breast imaging system producing glucose metabolic images using FDG. Journal of Nuclear Medicine. 2000; 41(11): 1851–1858. [PubMed: 11079494]

Ravindranath, B.; Maramraju, SH.; Junnarkar, SS.; Southekal, SS.; Stoll, SP.; Pratte, JF.; Purschke, ML.; Hong, X.; Bennett, D.; Cheng, K.; Tomasi, D.; Smith, DS.; Krishnamoorthy, S.; Vaska, P.; Woody, CL.; Schlyer, DJ. A simultaneous pet/mri breast scanner based on the ratcap; Nuclear Science Symposium Conference Record, 2008. NSS '08. IEEE; 2008; p. 4650-4655.

Raylman RR, Abraham J, Hazard H, Koren C, Filburn S, Schreiman JS, Kurian S, Majewski S, Marano GD. Initial clinical test of a breast-PET scanner. J Med Imaging Radiat Oncol. 2011; 55(1):58–64. [PubMed: 21382190]

Rosen EL, Turkington TG, Soo MS, Baker JA, Coleman RE. Detection of primary breast carcinoma with a dedicated, Large-Field-of-View FDG PET mammography device: Initialexperience 1. Radiology. 2005; 234(2):527–534. [PubMed: 15671006]

Seidel, J.; Vaquero, J.; Barbosa, F.; Lee, I.; Cuevas, C.; Gandler, W.; Green, M. Performance characteristics of position-sensitive photomultiplier tubes combined through common x and y resistive charge dividers; Nuclear Science Symposium, 1999. Conference Record. 1999 IEEE; 1999a; p. 1488-9.

Shah KS, Farrell R, Grazioso R, Harmon ES, Karplus E. Position-sensitive avalanche photodiodes for gamma-ray imaging. Nuclear Science, IEEE Transactions on. 2002; 49(4):1687–1692.

Shah KS, Grazioso R, Farrell R, Glodo J, McClish M, Entine G, Dokhale P, Cherry SR. Position sensitive APDs for small animal PET imaging. Nuclear Science, IEEE Transactions on. 2004; 51(1):91–95.

Shao Y, Meadors K, Silverman RW, Farrell R, Cirignano L, Grazioso R, Shah KS, Cherry SR. Dual APD array readout of LSO crystals: Optimization of crystal surface treatment. IEEE Trans. Nucl. Sci. 2002; 49(3):649–654.

Smith MF, Majewski S, Weisenberger AG, Kieper DA, Raylman RR, Turkington TG. Analysis of factors affecting positron emission mammography (PEM) image formation. IEEE Transactions on Nuclear Science. 2003; 50(1):53–59.

Springer A, Mawlawi OR. Evaluation of the quantitative accuracy of a commercially available positron emission mammography scanner. Medical Physics. 2011; 38(4):2132–2139. PMID: 21626946. [PubMed: 21626946]

Tai YC, Wu H, Pal D, O'Sullivan JA. Virtual-pinhole PET. J Nucl Med. 2008; 49(3):471–9. [PubMed: 18287272]

Thompson CJ. Feasibility study for positron emission mammography. Medical Physics. 1994; 21(4): 529. [PubMed: 8058019]

Wahl RL, Cody RL, Hutchins GD, Mudgett EE. Primary and metastatic breast carcinoma: initial clinical evaluation with PET with the radiolabeled glucose analogue 2-[F-18]-fluoro-2-deoxy-D-glucose. Radiology. 1991; 179(3):765–70. [PubMed: 2027989]

Wang GC, Huber JS, Moses WW, Qi J, Choong WS. Characterization of the LBNL PEM camera. Ieee Transactions on Nuclear Science. 2006; 53(3):1129–1135.

Weinberg, I.; Beylin, D.; Yarnall, S.; Anashkin, E.; Stepanov, P.; Dolinsky, S.; Zavarzin, V.; Peter, W.; Lauckner, K.; Morton, K.; Freimanis, R.; Lesko, N.; Levine, E.; Perrier, N.; Lovelace, J.; Geisinger, K.; Williams, R.; Wollenweber, S.; Narayanan, D.; Doss, M.; Hummel, J.; Sigurdson, E.; Evers, K.; Torosian, M.; Adler, L. Applications of a PET device with 1.5 mm FWHM intrinsic spatial resolution to breast cancer imaging; Biomedical Imaging: Nano to Macro, 2004. IEEE International Symposium on; 2004; p. 1396-1399.

Wu Y, Bowen SL, Yang K, Packard N, Fu L, Burkett G, Qi J, Boone JM, Cherry SR, Badawi RD. PET characteristics of a dedicated breast PET/CT scanner prototype. Phys Med Biol. 2009; 54(13):4273–87. [PubMed: 19531852]

Wu, Y.; Yang, K.; Packard, N.; Fu, L.; Stickel, J.; Tran, V.; Qi, J.; Boone, J.; Cherry, S.; Badawi, R. Characteristics of the PET component of a dedicated breast PET/CT scanner prototype; Nuclear Science Symposium Conference Record, 2006. IEEE; 2006; p. 2335-2339.

Yang Y, Dokhale PA. Depth of interaction resolution measurements for a high resolution PET detector using position sensitive avalanche photodiodes. Physics in Medicine and Biology. 2006; 51(9): 2131–2142. [PubMed: 16625031]

Yang YF, Wu YB, Qi JY, James SS, Du HN, Dokhale PA, Shah KS, Farrell R, Cherry SR. A prototype PET scanner with DOI-encoding detectors. J. Nucl. Med. 2008; 49(7):1132–1140. [PubMed: 18552140]

Yang Y, James SS, Wu Y, Du H, Qi J, Farrell R, Dokhale PA, Shah KS, Vaigneur K, Cherry SR. Tapered LSO arrays for small animal PET. Physics in Medicine and Biology. 2011; 56(1):139. [PubMed: 21119228]

Yang Y, Wu Y, Cherry SR. Investigation of depth of interaction encoding for a pixelated LSO array with a single Multi-Channel PMT. Nuclear Science, IEEE Transactions on. 2009; 56(5):2594–2599.

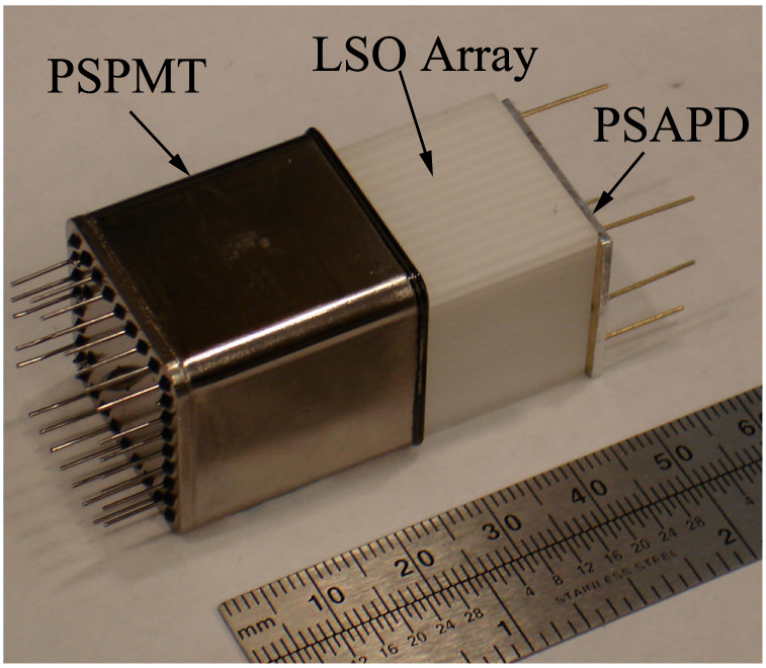

Figure 1.
Photograph of detector configuration. The external reflector is absent on the LSO array to facilitate visualization of the crystal elements.

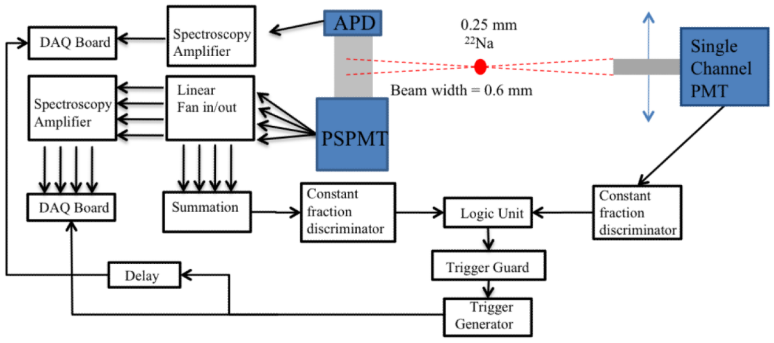

Figure 2.
Schematic of the depth of interaction experimental setup.

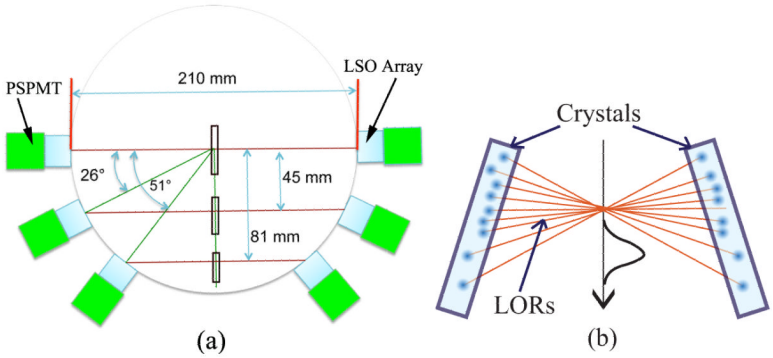

Figure 3.

(a) Intrinsic spatial resolution measurement setup. The black rectangles indicate the range of the point source positions used to measure the point-spread-function for each configuration. (b) DOI information from each crystal was used to calculate the photon interaction position and back-project the corresponding line of response. The ISR with DOI was estimated from the distribution of a profile through the focal plane of the reconstructed point source.

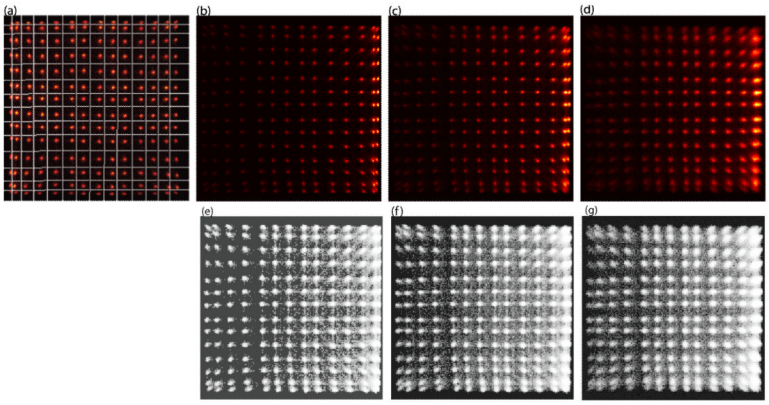

Figure 4.
Flood histograms showing the crystal array identification. (a) all depths with automated segmentation overlay. This flood was obtained from the timing resolution data set. (b) 2 mm depth nearest to the PSPMT. (c) 10 mm center depth. (d) 18 mm depth nearest to the PSAPD. (e)-(g) Histogram equalization was applied to (b)-(d) using the MatLab function "histeq"; for better viewing of crystals with fewer histogram counts.

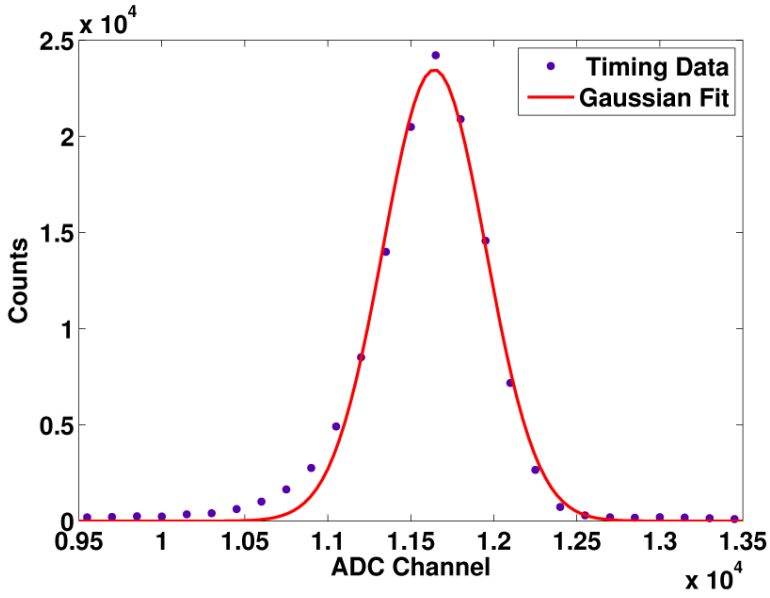

Figure 5.
Coincidence timing spectrum for the entire array. The FWHM is 2.4 ns.

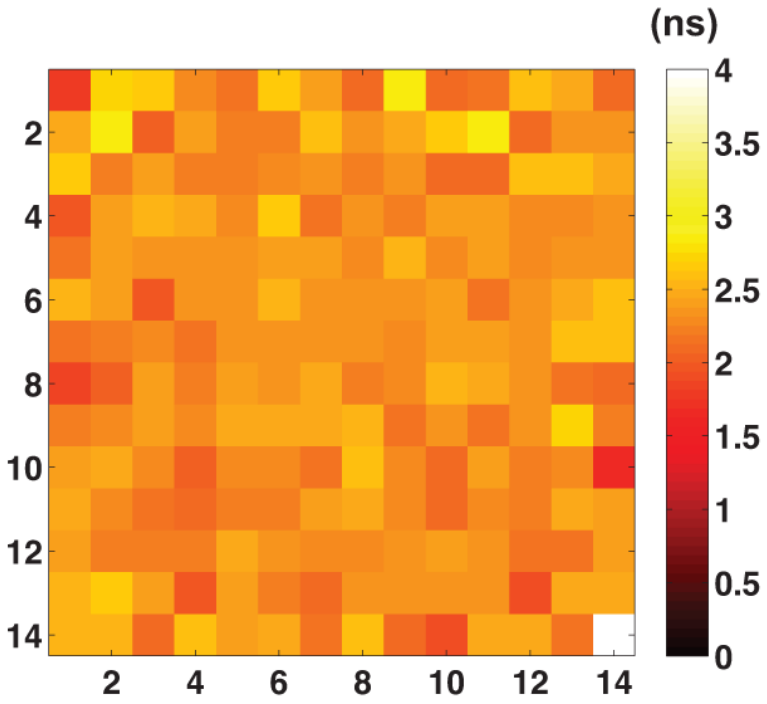

Figure 6.
Coincidence timing resolution crystal by crystal for the entire array. The mean timing resolution averaged across all crystals is 2.3 ns with a standard deviation of 0.20 ns.

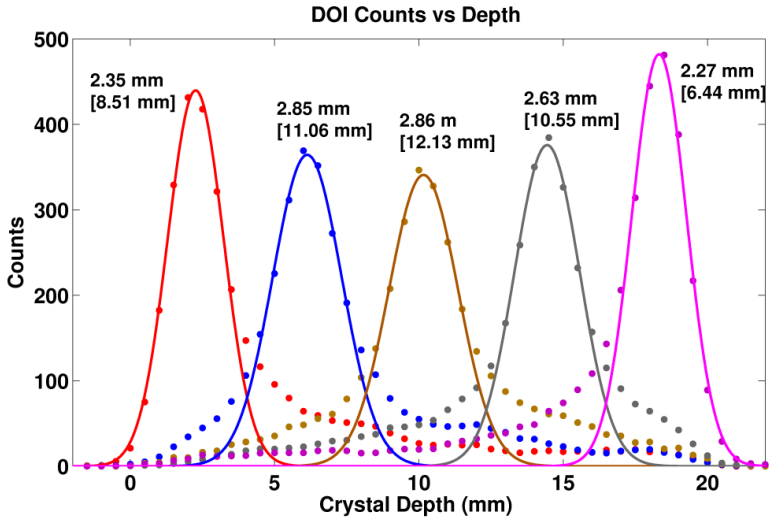

Figure 7.
DOI profiles for a single center crystal. The FWHM is shown for each profile with the FWTM shown in brackets. APD side is at 20 mm and the PSPMT side is at 0 mm. This orientation is used for all DOI measurements.

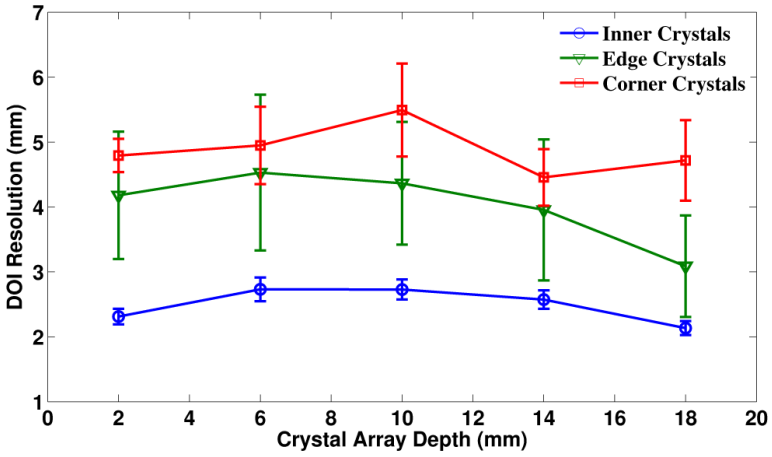

Figure 8.

The mean DOI resolution across crystals for three crystal groups: inner crystals, edge crystals, and corner crystals. The error bars indicate the standard deviation across crystals in a given group. The DOI resolution averaged across crystals and depths for each crystal group is: 2.4 mm, 4.0 mm, and 4.8 mm, respectively.

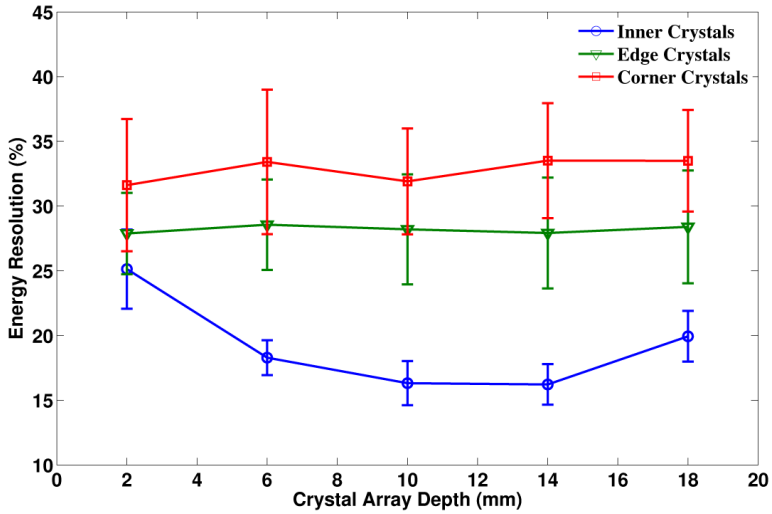

Figure 9.

The mean energy resolution across crystals for three crystal groups: inner crystals, edge crystals, and corner crystals. The error bars indicate the standard deviation across crystals in a given group. The energy resolution averaged across depths for each crystal group is: 19.1%, 28.2%, and 32.8 %, respectively.

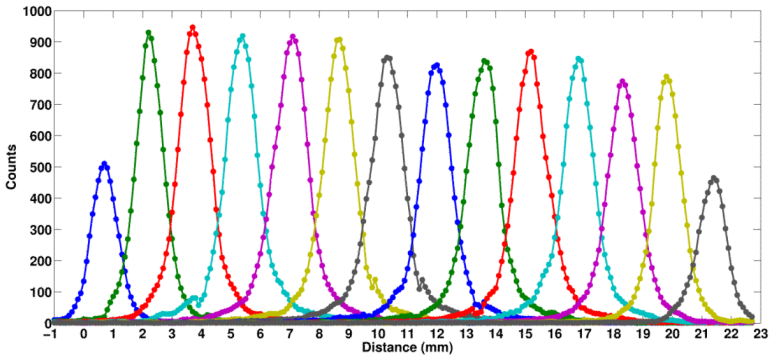

Figure 10.
Intrinsic spatial resolution at the center of the FOV. The mean ISR is 1.2 mm with a range of 1.1 mm - 1.3 mm and the corresponding mean FWTM is 2.66 mm with a range of 2.0 mm - 2.9 mm.

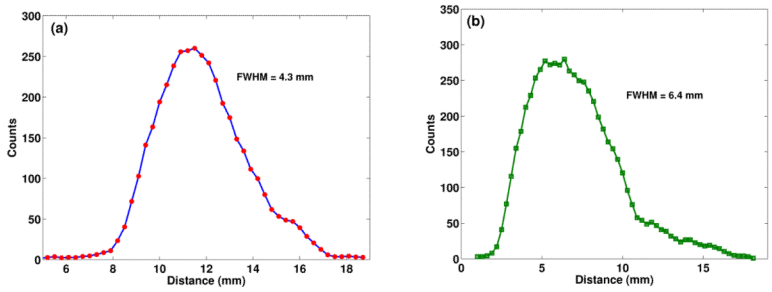

Figure 11.
ISR without DOI correction for a crystal in the central row of the crystal array. (a) at 26° oblique the FWHM is 4.3 mm and the FWTM is 8.2 mm. (b) at 51° oblique the FWHM is 6.4 mm and the FWTM is 10.9 mm .

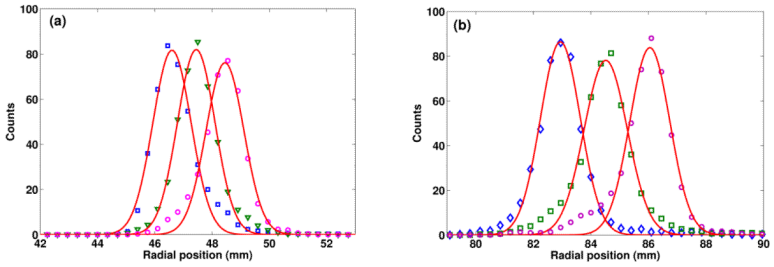

Figure 12.

ISR with DOI correction at oblique incidence photon angles. (a) at 26° the mean FWHM is 1.5 mm and the mean FWTM is 3.3 averaged across three source positions separated by 1 mm displacements. (b) at 51° the mean FWHM is 1.7 mm and the mean FWTM is 3.8 averaged across three source positions separated by 2 mm displacements. For measurement geometry see figure 3.

Table 1

Mean DOI and energy resolution values for two separate detectors averaged across crystals and depths in each array. The values in parenthesis is the standard deviation across crystals and depths. The columns “Inner crystals” corresponds to the 12 ×12 inner crystals.

	Detector 1		**Detector 2**	
Parameter	inner crystals only	all crystals	inner crystals only	all crystals
DOI resolution	2.4 mm (0.14mm)	2.9 mm (0.89 mm)	2.5 mm (0.23 mm)	3.1 mm (1.9 mm)
Energy resolution	19.1 % (1.2 %)	21.6 % (5.1 %)	20.4 % (2.8 %)	23.2 % (5.7 %)

Table 2

Results for repeatability of DOI measurement. The values are averages of all the crystals in the array.

Parameter	Measurement 1	Measurement 2	Measurement 3	Standard Deviation
DOI resolution	3.1 mm	2.9 mm	3.1 mm	0.12 mm
Energy resolution	20.9 %	20.4 %	21.6 %	0.64 %